

Generating Frequency Selective Vibrations in Remote Moving Magnets

Federico Masiero, Eliana La Frazia, Valerio Ianniciello, and Christian Cipriani*

Extensive efforts in providing upper limb amputees with sensory feedback have primarily focused on the restoration of tactile capabilities, while challenges in evoking proprioceptive sensations have been poorly addressed. Previously, an human-machine interface (HMI) was proposed based on permanent magnets implanted in residual muscles of an amputee, namely the myokinetic interface, to control robotic limb prostheses. Besides control, implanted magnets offer an unprecedented opportunity to trigger musculotendon proprioceptors via untethered selective vibrations. Herein, the challenge of tracking multiple moving magnets is addressed (e.g., following muscle contractions) while being vibrated by controlled magnetic fields produced by external coils. Results demonstrate the viability of a real-time (RT) system capable of simultaneously tracking and vibrating multiple moving magnets within a three-dimensional workspace. Highly selective torsional vibrations in the frequency span eliciting movement illusions (70, 80, and 90 Hz) are achieved on two moving magnets, with efficiencies above 0.82 (over 80% of spectral power at the desired frequency). Tracking accuracy and precision remain robust to the coil magnetic field, with position median errors below 1.2 mm and median displacement errors below 0.95 mm. This study represents a crucial step towards the development of a bench system to study proprioception in humans.

dexterous and sophisticated,^[1] the development of a functional and intuitive human-machine interface (HMI) to control those devices remains a long-standing challenge which is daily faced by researchers in the prosthetic field.^[2,3] In its ideal form such HMI includes: 1) a control component to interpret the user's motor intentions and send commands to an artificial arm or hand (efferent path),^[4] and 2) a sensory feedback component to sense the intrinsic status of the limb (proprioception) or its extrinsic interactions with the environment (exteroception), and to convey such information to the user (afferent path).^[5]

Research efforts in the field of sensory feedback, struggled in replacing tactile sensation with several non-invasive stimulation strategies, like vibro-, mechano-, or electro-tactile feedback,^[5-7] or direct electrical nerve stimulation.^[8-11] In addition to the sense of touch, a crucial component of somatosensation for motor planning and coordination is proprioception, i.e., the sense of the relative spatial position and movement of one's own body parts.

1. Introduction

Effective control methods and feedback strategies for upper limb prostheses has emerged among the top priorities in order to restore the natural sensory-motor control loop of amputees. Indeed, although prosthetic limbs have become increasingly


Other than helping refine movements in space, proprioception contributes to the sense of self-awareness in performing voluntary actions without necessarily relying on visual or auditory cues, namely the agency. Proprioception is tightly connected to the sense of joint movement or kinesthesia, which can be studied in humans by non-invasively applying 90 Hz vibrations from the skin to muscles or tendons.^[12] Such a technique, called kinesthetic or movement illusion, can trigger proprioceptors responses (naturally present in muscles and tendons), and was recently exploited by Marasco and colleagues in people with targeted muscle and sensory reinnervation, demonstrating improvements in upper limb prosthetic control.^[13,14]

We proposed the concept of a HMI that exploits the tracking of permanent magnets implanted inside residual muscles, as a real-time (RT) direct measure of their physical contraction, to control the movements of a prosthetic or assistive device. We dubbed it the myokinetic control interface.^[15,16] Besides control, our HMI offers the possibility of delivering kinesthetic sensations by selectively vibrating the implanted magnets using magnetic actuation. We referred to this idea as the myokinetic stimulation interface (Figure 1A).^[17,18]

Magnetic actuation is achieved by producing motion on (target) magnetic objects, such as magnets or magneto-responsive materials, through the interaction of their magnetic fields with

F. Masiero, E. La Frazia, V. Ianniciello, C. Cipriani
The BioRobotics Institute
Scuola Superiore Sant'Anna
Pisa 56127, Italy
E-mail: christian.cipriani@santannapisa.it

F. Masiero, E. La Frazia, V. Ianniciello, C. Cipriani
Department of Excellence in Robotics and AI
Scuola Superiore Sant'Anna
56127 Pisa, Italy

 The ORCID identification number(s) for the author(s) of this article can be found under <https://doi.org/10.1002/aisy.202300751>.

© 2024 The Authors. Advanced Intelligent Systems published by Wiley-VCH GmbH. This is an open access article under the terms of the Creative Commons Attribution License, which permits use, distribution and reproduction in any medium, provided the original work is properly cited.

DOI: 10.1002/aisy.202300751

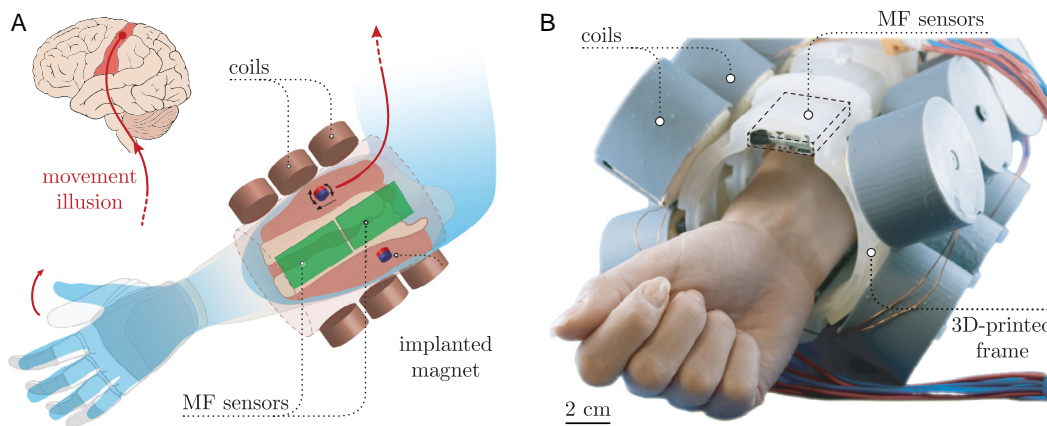


Figure 1. The myokinetic stimulation interface. A) Magnets implanted in muscles, which move following muscle contractions, are tracked (with an array of MF sensors) and remotely vibrated (e.g., using external coils) to provide feedback.^[17] B) Coil-array prototype of the myokinetic stimulation interface, consisting of 12 coils arranged in a cylindrical workspace fitting a 99th percentile forearm.

the remote magnetic fields generated by several sources.^[19] In its most common configuration, a magnetic actuation system uses multiple electromagnets (or coils) distributed around the workspace where the target objects are being manipulated. Alternatively, they may also use one or multiple sources mounted as the end-effectors of robotic arms/manipulators.^[19,20] Nonetheless, to finely control the produced magnetic field the knowledge of the pose (namely, the position and orientation in space) of the target objects is fundamental. Methods to retrieve the poses of the remote targets span from direct visual feedback using cameras, when there is a free line-of-sight,^[21–23] to ultrasound,^[24–26] X-ray^[27,28] or magnetic resonance instruments^[29–31] when the objects are occluded (like in the case of intra-body applications). However, none of these solutions are yet suitable for a clinically viable HMI.

A technically elegant solution would be to combine magnetic tracking with magnetic actuation techniques: one could indeed retrieve the poses of the targets by sensing the magnetic field using matrices of (Hall effect) sensors and computing the poses through nonlinear optimization.^[32] Such a choice is technically challenging, as it implies a sensing apparatus sensitive enough to the subtle magnetic fields produced by the targets but neither saturating nor exhibiting hysteresis under the large fields produced by the actuation sources.^[33] Thus, disentangling the magnetic fields produced by targets and sources imposes design tradeoffs at the sensor level (full-scale vs. sensibility),^[34] physical arrangement,^[35] modeling,^[36] or temporal multiplexing of the system tasks. Along these lines, some groups demonstrated successful pose estimation by embedding sensors and a power supply in the target (a robotic capsule for colonoscopy).^[37–39] Other groups reached similar results for a single target by finely modelling all the magnetic components.^[40–44] Alternatively, one could temporally multiplex tracking and actuation if the aggregated time required for the two processes is compatible with the final application; to the best of our knowledge, this approach has never been reported so far.

In our previous studies, we demonstrated a magnetic actuation system, capable of delivering selective vibrations to

multiple magnets.^[17] The poses of the magnets were retrieved once at power-on and assumed static during the system operation. Yet, this assumption is weak when considering targets that move in space, as in our application, where the magnets would displace following muscle contractions. Here, we present a RT system (Figure 1B) including the magnetic tracking and actuation and demonstrate its viability in simultaneously tracking and vibrating target magnets, being moved within a three-dimensional workspace. The system regulates the currents that flow through coils to generate controlled vibrations in the magnets, based on their localized pose, retrieved using matrices of hall-effect sensors (Figure 2).

Assessed through several actuation and tracking tests, the system proved capable of selectively vibrating slowly moving magnets while simultaneously tracking up to four.

Torsional vibrations in the frequency span eliciting movement illusions (i.e., 70, 80, and 90 Hz) on two moving magnets demonstrated highly selective, with efficiencies above 82%, while the tracking accuracy and precision proved robust enough to the MF of the coils (position median tracked error <1.2 mm in static vibrations with 2 magnets, displacement median error <0.95 mm). These outcomes represent an essential step forward towards the deployment of a novel scientific instrument capable to deliver proprioceptive feedback in persons with implanted magnets in their muscles. Moreover, this study significantly contributes to the several scientific and technological open challenges in magnetically actuating remote moving targets.

2. Experimental Section

2.1. System Architecture

The system was designed as a bench device to induce sinusoidal vibrations within the frequency range eliciting kinesthetic illusions (70–90 Hz range)^[13] into remote slowly moving magnets, by controlling the compound external MF interacting with them (and generated by currents flowing into coils), and by updating it with the RT information of the retrieved magnet poses.

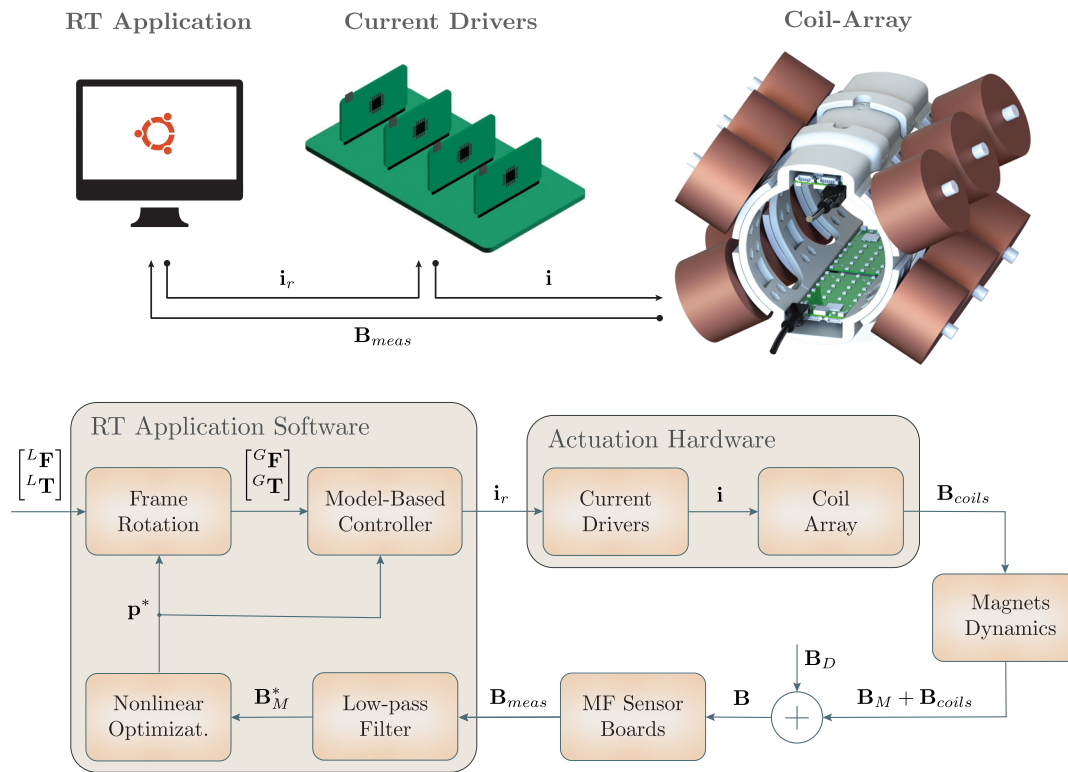


Figure 2. System architecture and control scheme. A real-time (RT) application computes the currents i_r to vibrate the magnets and sends this information to the current drivers, which feed the coil-array with the appropriate currents. In detail, in the RT application a vibration reference is transformed from the local $([F^L, T^L]^T)$ to the global $([F^G, T^G]^T)$ frame and the corresponding i_r is computed through the model-based controller. Based on it, the current drivers feed the coil array with a current i generating a magnetic field and, consequently, vibrating the magnets. The compound MF of magnets (B_M), coils (B_{coils}), and external disturbances (B_D) is collected by MF sensors boards (B_{meas}) and low-pass filtered (B_M^*) to track the magnets pose (p^*) via nonlinear optimization.

The system comprised: 1) a personal computer (PC), 2) 12 cylindrical coils arranged around a cylindrical workspace (coil-array, sized as a 99th percentile human-forearm), supplied by commercial current drivers (MC5004, Faulhaber Minimotor SA, Switzerland), 3) the remote magnets (up to 4), and 4) four MF sensor boards mounting a grid of 20 3-axis magnetometers (LIS3MLD, STMicroelectronics, Switzerland) (Figure 1B).^[45]

The PC runs a RT C++ application (Ubuntu Linux with RT-PREEMPT patch) that implements the control algorithm through a three-step iterative procedure: 1) acquires and filters the MF collected by the sensor boards, 2) implements the tracking algorithm to retrieve the poses of the slowly moving magnets, and 3) uses this information to update a model-based controller (Figure 2). Specifically, the sensor boards sample and send to the PC (360 Hz rate) the MF which is generated by the magnets and coils acting in the workspace. This data is low-pass filtered (3rd order Butterworth, 3 Hz cut-off frequency), under the hypothesis that any movement of the magnets is quasi-static with respect to the excitation frequency of the coils (and this assumption holds true when considering human movements),^[46] and fed to the tracking algorithm. The latter employs the Levenberg–Marquardt algorithm (LMA)^[47] to estimate the magnet poses from the pre-processed MF measures (60 Hz tracking rate).^[32] The model-based controller uses the dipole–dipole

interaction^[17] to compute the current references (500 Hz control rate) from the retrieved poses. The current references are thus sent to the current drivers (which implement a low-level proportional-integrative control on the current), to apply magnetic torques and forces to the remote magnets, inducing the desired behavior (keeping still or vibrating them).

2.2. Simulations

The power demand of the system when delivering amplitude-modulated vibrations within its workspace was assessed by means of the current root mean square (RMS) value, in simulation (Figure 3). In fact, while it is possible to produce theoretically arbitrary MFs in space,^[19,20] their actual implementation depends on the geometrical configuration of the MF elements, as well as hardware limits, among which the maximum currents allowed by the coils, drivers, and power source. Consequently, the workspace of systems like these is very likely to be anisotropic in terms of vibration capabilities. The spatial arrangement of the coils and remote magnets was thus modeled using MATLAB (The MathWorks Inc, Natick, USA), with the magnets spanning across a 3D grid (of 1 mm step resolution) within a hollow cylinder inside the workspace ($r_{in} = 10$ mm, $r_{out} = 30$ mm and $l = 120$ mm) (Figure 3A). Two sets of simulations were carried

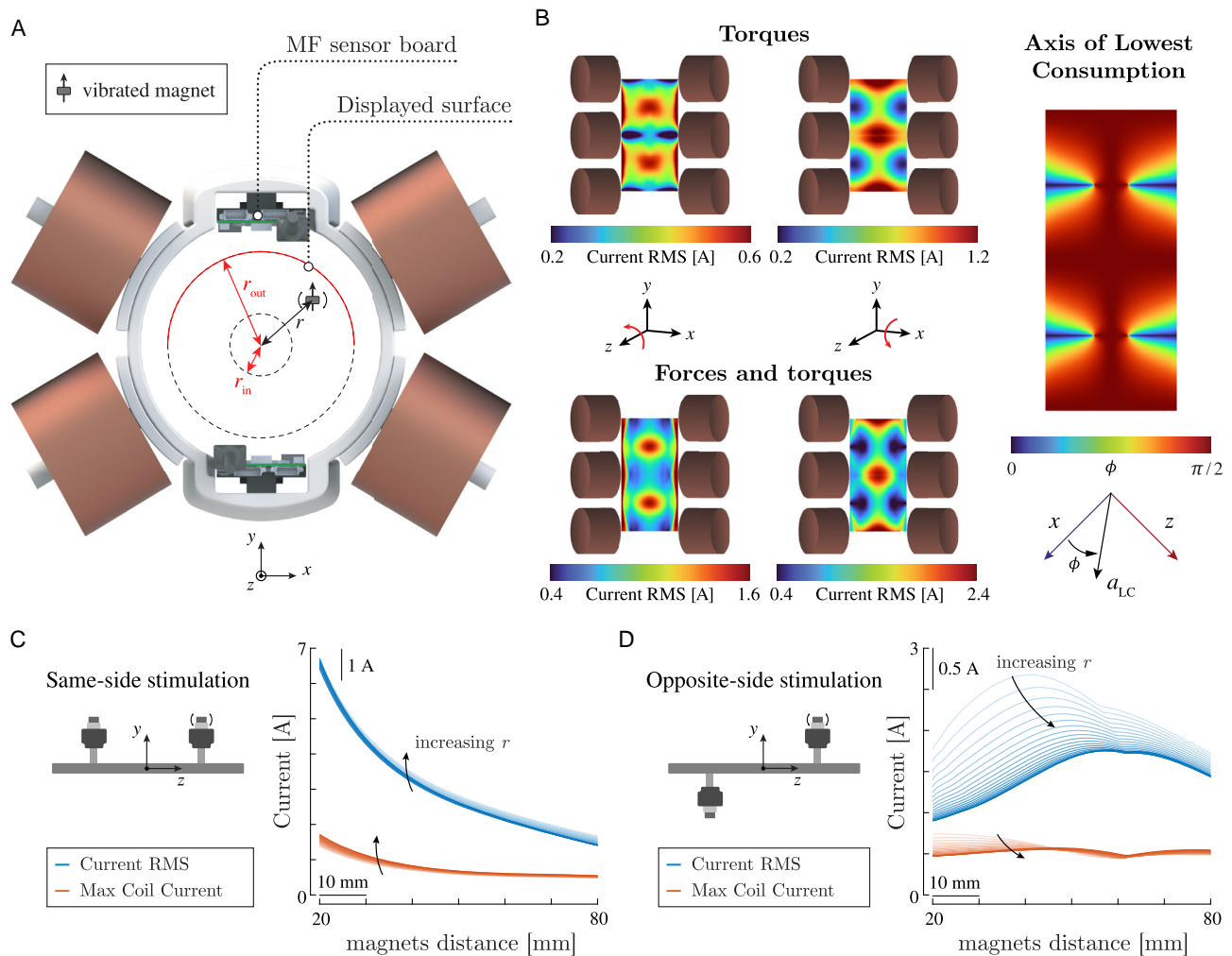


Figure 3. Simulation results. A) Simulations setup with 1 vibrated magnet. The red curve marks the displayed surface in the results. B) Current RMS values computed by the model-based controller for: torque vibrations about the z axis (top left) and the x axis (top right) of the system, simultaneous torque and force vibrations about the z axis (bottom left) and the x axis (bottom right). The contour at the right shows the axis of lowest consumption, a_{LC} , and displays it as its angle w.r.t. the x axis (e.g., $\phi = \pi/2$ means that a_{LC} is aligned with z). C, D) provide the arrangement for the 2-magnets simulation setups (left) and the resulting current RMS values and maximum coil current computed by the model-based controller as a function of the inter-magnet distance and the radial distance from the workspace center, r .

out with either 1) a single or 2) a pair of magnets oriented towards the sensor boards (Figure 3A). Those with a single magnet were carried out for multiple vibration axes and considering both purely torque vibrations ($20 \mu\text{Nm}$ peak-to-peak amplitude) and simultaneous force-torque vibrations ($20 \mu\text{Nm}$ peak-to-peak amplitude, and null force) (Figure 3B). Notably, the latter still consisted in delivering torsional vibrations but with more control over the magnet centroid (imposing no translations).^[17] With pair of magnets, instead, the simulation considered purely torque vibrations only, under two conditions that delineate the boundaries of all possible combinations: with the magnets in the same workspace region (*same-side stimulation*, Figure 3C) or on opposite sides (*opposite-side stimulation*, Figure 3D). The current RMS value was evaluated for different distances between magnets (20–80 mm), on longitudinal axes at a radial distance r (10–30 mm) from the center.

2.3. Experimental Measurements

The actual viability of the system in finely vibrating slowly moving magnets, or in other words, in tracking their poses and updating the vibration in the model-based controller, was verified within a workspace sized as the human forearm. To this aim, disk magnets (NdFeB N52 grade, axial magnetization, 4 mm diameter, 2 mm height), rigidly attached on a substrate of viscoelastic material resembling the stiffness of muscular tissue (cylinder: 5 mm diameter, 4 mm height, using Ecoflex 00-30, Smooth-On Inc., Pennsylvania, USA), were used.^[48] In the first batch of tests, the actual physical oscillations of the magnets were assessed using image processing algorithms and a high-speed video camera (Test A – video analysis). Then, a comprehensive characterization of the workspace and the effects of the actuation MFs on the tracking accuracy and precision of the magnetic

tracking algorithm were measured, for both a single and a pair of magnets (Test B - effects of actuation on the tracking accuracy and precision). The errors determined by the actuation MFs, were computed from the poses estimated with and without the induced vibrations. In all tests, the magnet(s) poses were continuously tracked with the LMA and used to update the model-based control algorithm in order to deliver purely torque vibration with up to $80 \mu\text{Nm}$ of peak-to-peak amplitude (corresponding to the maximum hardware limit).

2.3.1. Test A – Video Analysis

A high-speed video camera (Sony DSC-RX10M4; 1000 fps maximum frame rate, with a 1080p maximum resolution) and image processing algorithms were used to assess performance of the system in generating selective vibrations (in terms of frequency and magnet selectivity) over two slowly moving magnets (Figure 4). One of the magnets was vibrated using sinusoidal

torque profiles (peak-to-peak amplitude: $40 \mu\text{Nm}$; 70, 80, 90 Hz frequency range) about the axis perpendicular to the plane of the camera (z axis, Figure 4A), while the other magnet was kept still, akin our previous study.^[18] The test was repeated with the magnets moving along a linear trajectory parallel to the camera plane (1.5 cm s^{-1} speed, x axis), and with static magnets as a control condition (Figure 4A).

The videos were processed frame by frame (MATLAB Image Processing Toolbox) to gather magnets motion information via blob analysis. Specifically, each video frame was converted to grayscale, transformed into a binary image (thresholding), and processed through a sequence of filtering (gaussian smoothing and edge detection) and morphological operations to reconstruct the orientation and position of magnets centroids, namely their planar absolute pose. The spectrum and the power spectral density (PSD) of each signal was calculated to extract: P_{ang} and $P_{\text{ang}f}$, i.e., the power of the displacement signal about the rotation direction, in the whole spectrum and at the frequency

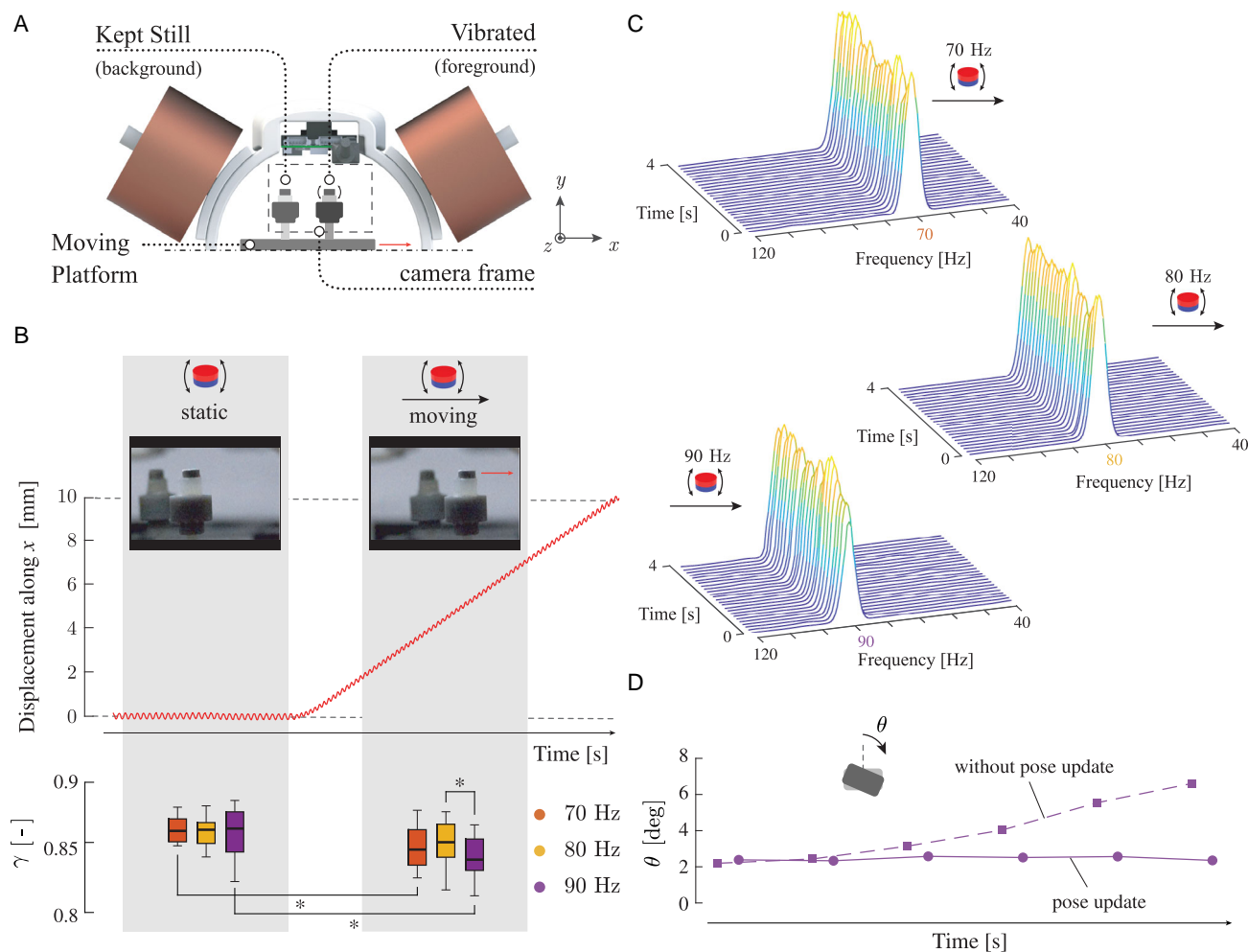


Figure 4. Frequency selectivity. A) Experimental setup for the video analysis. Two magnets displaced by a moving platform parallel to the camera plane while they were controlled: one magnet was vibrated (70, 80, 90 Hz), while the other was kept still. B) Comparison of torsional efficiency, γ , when the magnet was static and when it was moving ($*P < 0.05$, $**P < 0.01$). C) Sample power spectra of the angular displacement of the vibrated magnet during the motion test at 70, 80, and 90 Hz. D) Amplitude vibration of the magnet controlled with and without pose update. Whiskers in box plots show the minimum and maximum data values after disregarding the outliers (i.e., those values below $Q1 - 1.5 \times IQR$ and above $Q3 + 1.5 \times IQR$).

of interest, respectively. These were used to assess the torsional efficiency of the system according to the following equation:

$$\gamma = P_{\text{anglf}}/P_{\text{ang}}$$

Moreover, to assess the system performance in more challenging scenarios, additional tests were performed with 1) two magnets following piece-wise linear trajectories, or 2) with four static magnets, while vibrating one of them and keeping fixed the others. Finally, the qualitative behavior of the system with and without the update of the magnet poses were demonstrated.

2.3.2. Test B – Effects of Actuation on the Tracking Accuracy and Precision

Test B1 – Single Static Magnet: The effects of the actuation MFs on the tracking accuracy and precision of a single magnet (M_1) were assessed while varying the: 1) vibration axis, 2) amplitude of vibration, and 3) position in the workspace (**Figure 5**). More in detail, one magnet was vibrated at 90 Hz, under torque control, in four different ways, which combined the vibration axis (axes x and z , perpendicular to the magnet magnetization vector, Figure 5) and the peak-to-peak amplitude (40 and 80 μNm). The test was repeated with the magnet placed in 120 points of a 3D grid ($18 \times 8 \times 80 \text{ mm}^3$) within a human-forearm-sized workspace, with the magnetization axis always pointing towards the sensor boards. For each condition, the pose was recorded for 5 s, resulting in approximately 300 pose samples.

Calling $\mathbf{P}_{\text{act_on}}$, $\mathbf{O}_{\text{act_on}}$ the position and orientation tracked while vibrating the magnet, and $\mathbf{P}_{\text{act_off}}$, $\mathbf{O}_{\text{act_off}}$ the same

quantities without vibrations, the errors induced by the actuation MFs, were computed via Equation (1) and (2), as:

$$\Delta e_P = \mathbf{P}_{\text{act_on}} - \mathbf{P}_{\text{act_off}} \quad (1)$$

$$\Delta e_O = \cos^{-1}(\mathbf{O}_{\text{act_on}} \cdot \mathbf{O}_{\text{act_off}}) \quad (2)$$

where the orientations $\mathbf{O}_{\text{act_on}}$, $\mathbf{O}_{\text{act_off}}$ are expressed as the normalized (unit norm) magnetic moment vector of the magnet.

The medians (ΔE_P , ΔE_O) and inter-quartile range, IQR (ΔS_P , ΔS_O), of Δe_P and Δe_O were used to quantify the effects of the MF on the tracking accuracy and precision, respectively, akin to our previous studies.^[32,45]

Test B2 – Multiple Static Magnets: The effects of the actuation MFs on the tracking performance of two magnets (M_1 and M_2) were assessed while varying the relative distance between the magnets. One magnet was vibrated at 90 Hz, under torque control (40 and 80 μNm peak-to-peak amplitude), about the two axes perpendicular to the magnetization vectors, while the other one was kept still (**Figure 6**). The magnets, placed 15 mm far from the sensor boards, were distanced at 15 increasing distances (from 20 to 78 mm), with the magnetization axis always pointing towards the sensor boards. For each condition, 300 pose samples were collected. To extend the results with more than two magnets, similar tests were performed with four magnets (M_1, \dots, M_4) placed 15 mm far from the sensor boards, by vibrating one out of four (torque control, 40 μNm peak-to-peak amplitude). Similar to Test B1, also in this test we computed the errors induced by the actuation MFs with Equation (1) and (2) from

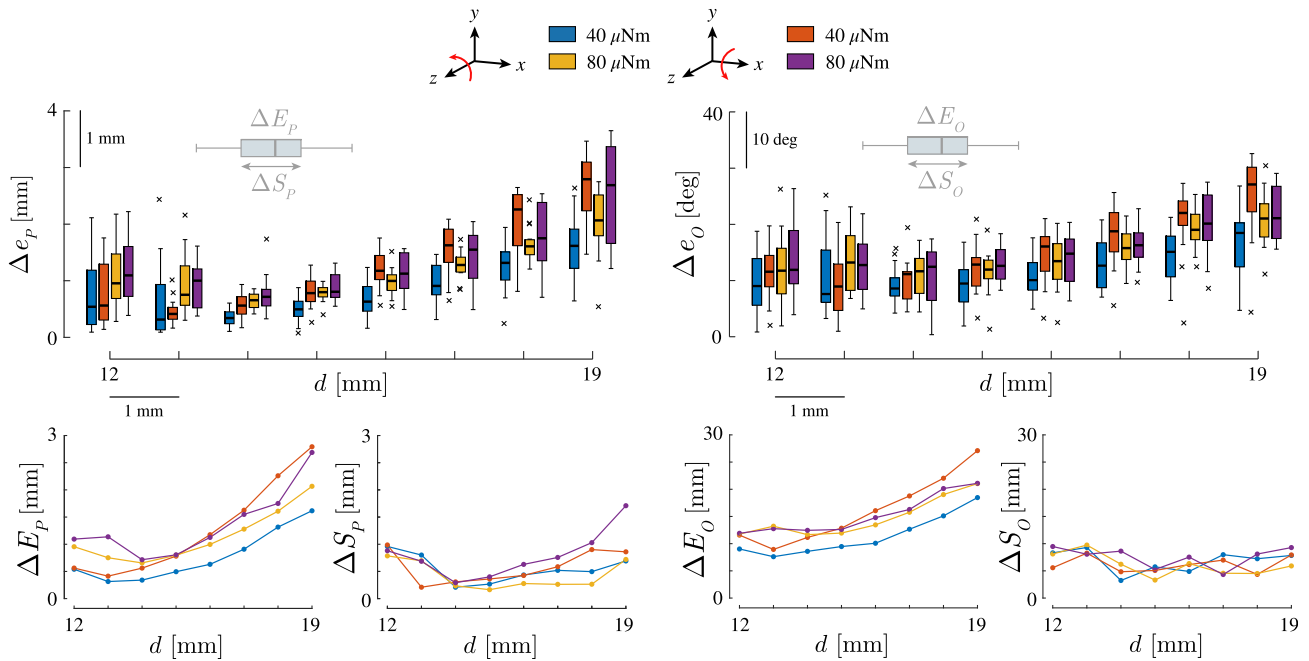


Figure 5. Tracking errors for single static magnet. Position, Δe_P , and orientation, Δe_O , errors of localization of one magnet introduced by the vibration (the error is computed as the difference between the localization with and without vibration). The magnet was vibrated in 15 check points at 8 increasing distances from the sensor boards (12–19 mm), with different testing conditions for the vibrations, namely, two distinct actuation axes (z , x axis) and two amplitudes (40 and 80 μNm). Each boxplot provides the error distribution of all the points at a constant distance, d , from the sensor boards. Their corresponding medians (ΔE_P , ΔE_O) and inter-quartile ranges (ΔS_P , ΔS_O) are also reported in separate graphs. Whiskers in box plots show the minimum and maximum data values after disregarding the outliers (i.e., those values below $Q1 - 1.5 \times \text{IQR}$ and above $Q3 + 1.5 \times \text{IQR}$).

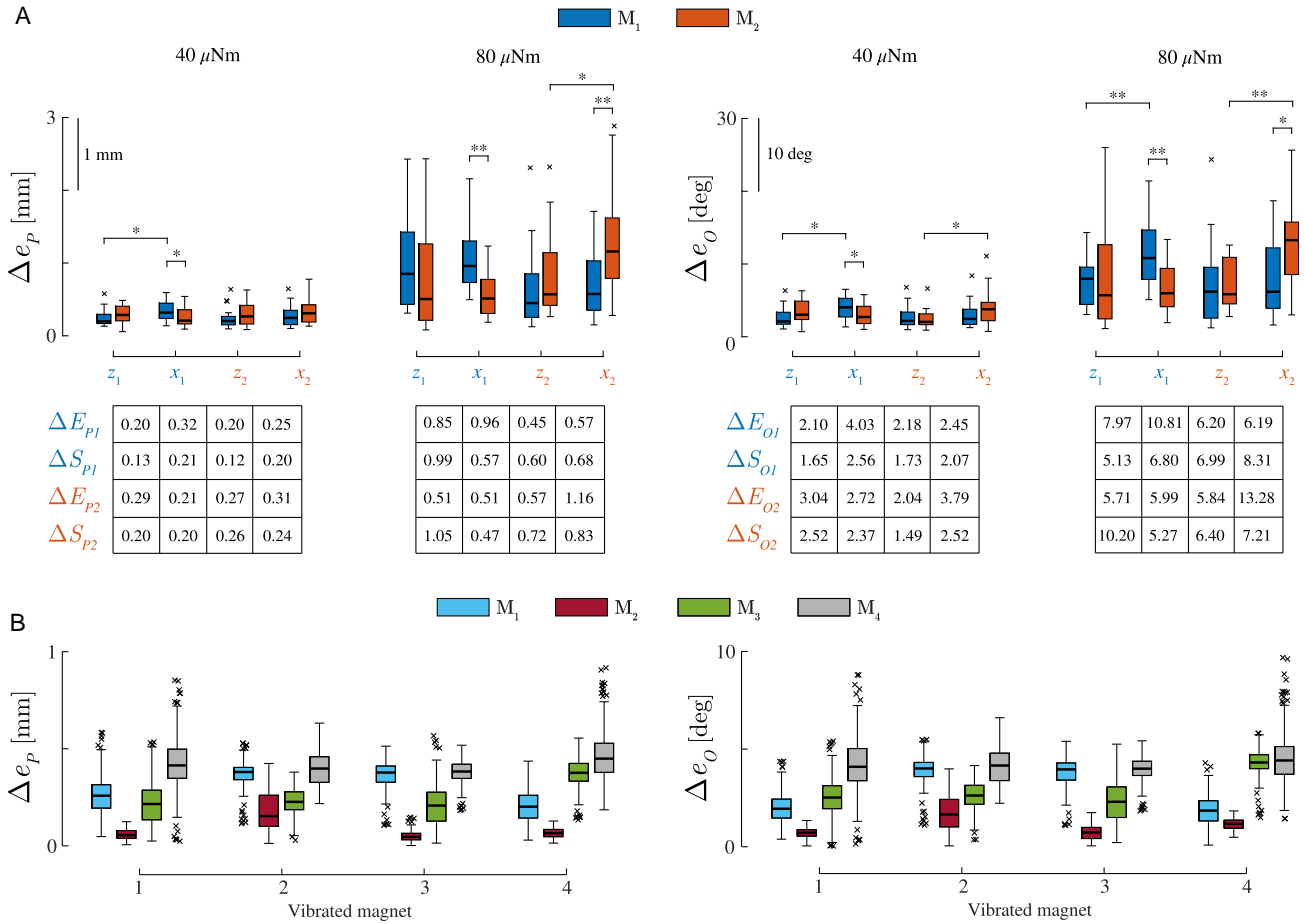


Figure 6. Tracking errors for multiple static magnets. Position, Δe_p , and orientation Δe_o errors of two A) and four B) magnets vibrated with the same testing conditions of Test B1 one at a time (red, blue). (A) Error distributions are shown w.r.t. the i) vibration axis (x, z), ii) vibration amplitude (40 and 80 μNm) and iii) selected magnet for a total of 8 conditions. Medians (ΔE_{pi} , ΔE_{oi}) and inter-quartile ranges (ΔS_{pi} , ΔS_{oi}), for each testing condition, are reported in the tables below each graph. Larger vibration amplitudes led to larger ΔE_{pi} , ΔE_{oi} and ΔS_{pi} , ΔS_{oi} . (B) Error distributions for four magnets are shown w.r.t. the vibration axis in the case of 40 μNm torque vibrations along z . Whiskers in box plots show the minimum and maximum data values after disregarding the outliers (i.e., those values below $Q1 - 1.5 \times \text{IQR}$ and above $Q3 + 1.5 \times \text{IQR}$).

the tracked position and orientation of each magnet in absence and presence of the induced vibrations.

Test B3 – Multiple Moving Magnets: The effects of the actuation MFs on the tracking performance of two magnets (M_1 and M_2) jointly moving along a linear trajectory (1.5 cm s^{-1} speed), parallel to the sensor boards, was assessed, while varying the travelled distance. One magnet was vibrated at 90 Hz, under torque control (40 and 80 μNm peak-to-peak amplitude), about the two axes perpendicular to the magnetization vectors, while the other one was kept still (Figure 7A). The magnets, placed 30 mm far each other, were moved along trajectories of increasing distance, mimicking the expected displacement induced by a muscle contraction: 2, 4, 6, 8, and 10 mm. Each trajectory was repeated 10 times.

The effects of the actuation MFs were assessed with the absolute value of the difference between the tracked displacements with actuation, $D_{\text{act,on}}$, and without actuation, $D_{\text{act,off}}$, as $|\Delta e_D| = |D_{\text{act,on}} - D_{\text{act,off}}|$ (note that this time, displacements rather than positions are considered, and Δe_D could indeed assume both negative and positive values).

2.4. Statistical Analysis

Statistical tests were performed using MATLAB. The Kolmogorov–Smirnov test was used to check the normality of the distributions. An unpaired t -test was used to assess statistical differences between torsional efficiency (γ) distributions while the vibrated magnet was moving and while it was not. Wilcoxon test assessed statistical differences between tracking error distributions (Δe_p , Δe_o) of two magnets. For all tests, P values are indicated in the figures as: * for $P < 0.05$ and ** for $P < 0.01$.

3. Results

3.1. Simulations

The computer simulations run to investigate the isotropy of the workspace proved that the current RMS value required by coils to induce vibrations to a single remote magnet was correlated with

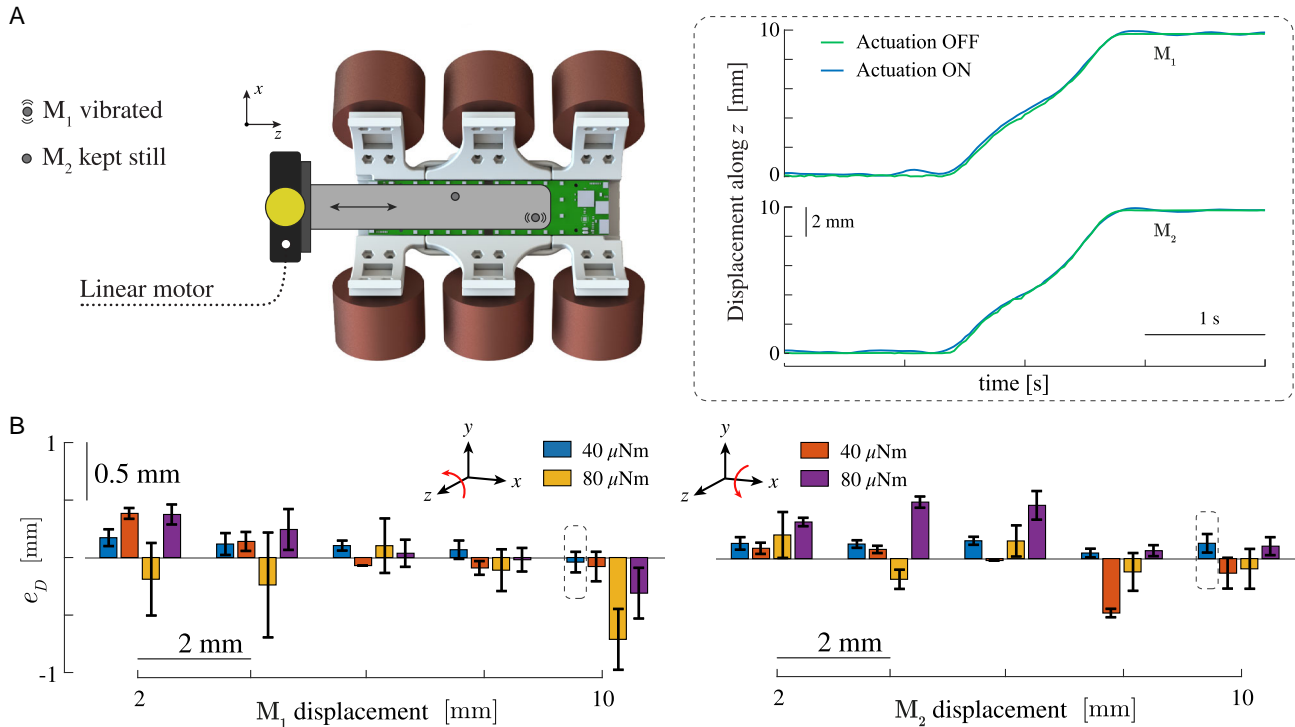


Figure 7. Simulating magnets contractions. A) Two magnets were simultaneously moved along the z axis (main workspace axis) thanks to a moving platform mimicking muscle contraction, while delivering purely selective torque vibrations (only to M_1) and simultaneously tracking both. On the right, a representation of the tracked displacements while the magnets were vibrated (Actuation ON) and while they were not (Actuation OFF). B) The displacement error, Δe_D , was computed as the difference between the tracked displacement with and without vibrations in four different conditions: mixing actuation axes (z, x) and amplitudes (40 and $80 \mu\text{Nm}$). The medians (ΔE_D) of ten repetitions per trajectory were computed and are shown as the edges of the bars, while whiskers indicate the interquartile range (ΔS_D) of the tracked displacement. Whiskers in box plots show the minimum and maximum data values after disregarding the outliers (i.e., those values below $Q1 - 1.5 \times \text{IQR}$ and above $Q3 + 1.5 \times \text{IQR}$).

their spatial arrangement (Figure 3). In the case of pure torque vibrations ($20 \mu\text{Nm}$ peak-to-peak amplitude) about the longitudinal axis (z axis), the RMS ranged from 200 mA in the workspace regions closer to the axis of the coils, to 600 mA in the grid points between them or farther from them (close to the sensor boards) (Figure 3B). The maximum value for vibrations about the x axis proved 1.2 A , but this time the locations of minimum and maximum current RMS were almost complementary. In the case of force and torque vibrations ($20 \mu\text{Nm}$ peak-to-peak amplitude, and null force) about the z axis, the RMS ranged from 400 mA in the workspace regions closer to the axes of the coils, to 1.6 A in the grid points closer and farther from them. The maximum value for vibrations about the x axis proved 2.4 A and was mostly located at the (upper and lower) boundaries of the workspace.

The z axis proved the direction of vibration exhibiting the lowest energy consumption on the xz plane, in almost the entire workspace (Figure 3B, $a_{LC}, \phi = \pi/2$), except for confined symmetric regions between the coils, where the optimal axis gradually became the x one in the regions equally far from adjacent coils.

When considering 2 magnets, significant differences were observed in the two conditions tested: same-side versus opposite-side stimulation (where the vibrated magnets were located on the same or opposite side of the workspace, respectively). In the former, the current RMS value proved negatively correlated with the

distance between magnets, ranging from 6.5 A (20 mm distance) down to 1 A (80 mm distance) (Figure 3C). These trends were minimally affected by the radial distance r from the main system axis, exhibiting a $\approx 0.5 \text{ A}$ variability from $r = 10$ to 30 mm . In the opposite-side stimulation condition, the current RMS value proved smaller (up to $\approx 2.6 \text{ A}$). For increasing values of r , the maximum current RMS value shifted towards increasing magnets distances (i.e., at a relative distance $\approx 60 \text{ mm}$, Figure 3D).

3.2. Test A – Video Analysis

The video analysis demonstrated the system capability of eliciting highly efficient vibrations in terms of frequency selectivity, both with static and slowly moving pairs of magnets (Figure 4B,C, Movie S1 and S2, Supporting Information). Indeed, the torsional efficiency, γ , ranged between 0.82 and 0.89 across the tested frequencies, meaning that at least 80% of the power spectrum of the vibration signal was located at the desired frequency. The efficiencies computed with static (≈ 0.87) and moving magnets (≈ 0.85) proved slightly yet significantly different ($P < 0.01$, two-sample unpaired t -test, Figure 4B). Irrespectively of the delivered vibration frequency ($70, 80, 90 \text{ Hz}$), the spectrum of the stimulus exhibited an almost constant amplitude for the entire motion of the magnets (representative examples in Figure 4C).

The efficacy of the system extended to the cases when the magnets moved following piece-wise linear trajectories (Movie S3, Supporting Information) or with four static magnets (Movie S4, Supporting Information). The pose update proved indeed crucial to maintain constant the vibration amplitude and the magnet selectivity during motion. In fact, when disabling the pose update uncontrollable vibrations were observed in the target magnet (Figure 4D and Movie S5, Supporting Information) and unintended vibrations in magnets different from the target one (Movie S6, Supporting Information).

3.3. Test B1 – Single Static Magnet

The MF generated by the coils to vibrate one magnet, produced errors in the tracked poses which were roughly proportional to the amplitude of the vibration, and with greater effects when vibrating about the x axis (Figure 5). More in detail, the median displacement in the tracked position (ΔE_p) and orientation (ΔE_o) displayed a non-monotonic trend w.r.t. the distance to the sensors, d . For instance, for 40 μNm torque vibrations about the z axis, the delta reached a maximum of 2.6 mm and 27°, and a minimum of ≈ 0.5 mm and $\approx 10^\circ$ at $d = 14$ mm. Similarly, ΔS_p exhibited a sort of parabolic trend, with values of the same order of magnitude, whereas ΔS_o did not exhibit a clear pattern.

3.4. Test B2 – Multiple Static Magnets

When inducing a vibration in one out of two magnets while forcing the other to stay still, the Δe_p and Δe_o did not change significantly across the several conditions (axis and vibrated magnet), when the torque amplitude was 40 μNm (Figure 6A). In this case, ΔE_p ranged between 0.2 and 0.32 mm, while ΔE_o between 2.04° and 4.03°. In contrast, with a torque of 80 μNm larger mis-localizations were observed as shown by a larger median value and dispersion of the tracked pose, with a greater effect on the vibrated magnet. Pairwise comparisons revealed statistically larger pose errors in the vibrated magnets with respect to the still ones, when actuating them about the x axis, in three cases out of four (Wilcoxon rank-sum test, $P < 0.05$) (Figure 6). Statistical differences were also sometimes observed when vibrating the same magnet about different actuation axes. For instance, focusing on Δe_p , larger errors were observed when vibrating M_1 at 40 μNm and M_2 at 80 μNm about the x axis.

When vibrating one out of four magnets (Movie S4, Supporting Information), at 40 μNm , the Δe_p and Δe_o proved greater than when vibrating one out of two, yet always below 0.9 mm and 9.6°, respectively (Figure 6B). In particular, the following ranges for ΔE_p and ΔE_o were found: 0.2–0.4 mm and 1.8–4° for M_1 , 0.05–0.1 mm and 0.7–1.7° for M_2 , 0.2–0.4 mm and 2.3–4.3° for M_3 , 0.4–0.5 mm and 4.0–4.4° for M_4 . More in general, in the areas of the workspace closest to the coils, some crosstalk vibration could be observed in the magnet closest to the vibrated one.

3.5. Test B3 – Multiple Moving Magnets

In tests with two moving magnets following a linear trajectory, while inducing one to vibrate and forcing the other to stay still, the effects of the actuation MF perturbed the tracking absolute position but did not alter that much the tracked displacement of the moving magnets. The median displacement error, ΔE_D , across all the tests was found to be always < 0.71 mm, with a maximum absolute error of 0.95 mm (Figure 7). The latter was found in the vibrated magnet while travelling a 10 mm trajectory influenced by an 80 μNm torque about the x axis. In particular, the effect of the actuation MF did not necessarily affect the tracking accuracy of the vibrated magnet but rather its precision. In fact, no clear pattern was found looking at the median errors of both magnets w.r.t. to amplitude of the vibration and axis choice: for example, when vibrating about the x axis with a 40 μNm torque, ΔE_D was significantly greater in opposite magnets when travelling 2 and 8 mm displacements. On the contrary, ΔS_D proved equal or lower in the still magnet, reaching its maximum of ≈ 0.8 mm in the vibrated one while travelling a 4 mm trajectory influenced by an 80 μNm torque about the x axis. Moreover, ΔS_D was also clearly affected by the axis choice and the torque amplitude as it increased for increasing amplitude and when the x axis was selected.

4. Discussion and Conclusions

Research in magnetic-based approaches applied to the industrial and medical fields are rapidly growing, and the corresponding technical and scientific advances in those methods are needed to translate laboratory prototypes to clinical deployment.^[49] Here, we presented a RT system able to selectively vibrate magnets (at 500 Hz control frequency) within a three-dimensional workspace while simultaneously tracking their poses (at 60 Hz). This was done by leveraging magnetic tracking and actuation technologies, thus bypassing the need of direct line of sight or other additional imaging systems (MRI coils, X-ray, or ultrasounds). Crucial component of the system functionality is the capability of rejecting the (disturbing) MF generated by the coils to vibrate the magnets from their MF readings, needed to retrieve the poses via nonlinear optimization. Unlike previous works, which included coils contributions in the tracking algorithm,^[41,44] in this study we combined the tracking system with the actuation one using a filter approach to disentangle the quasi-static MF generated by the magnets and the time-varying ones generated by the coils (Figure 2). To the best of our knowledge, the only study demonstrating simultaneous magnetic tracking and actuation in presence of time-varying MFs, uses echoes to generate magneto-mechanical resonance traces.^[50] We deemed our approach reasonable because the dynamics of the implanted magnets during self-paced contractions falls within 0.7–3 Hz range,^[46] i.e., much smaller than the target vibration frequencies adopted to trigger muscle proprioceptor responses.^[12]

The final system architecture (Figure 1B) represents an optimized version of our previous one^[17] in terms of power consumption and space requirements (i.e., to host the MF sensor boards around the cylindrical workspace). The simulations were used to characterize the power consumption (estimated via the

current RMS value) when vibrating a magnet in space in presence of purely torque and simultaneous force and torque vibrations (Figure 3). Not surprisingly, the current RMS value was not isotropic in the workspace and higher when both forces and torques were controlled. Consequently, purely torque vibrations were considered in all the experiments. In addition, the current demand depended on the axis of actuation: larger current RMS values were needed for vibrations about the \square axis, except for small regions between adjacent coils along the main workspace axis (Figure 3B).

The outcomes from the video analysis test (Test A) confirmed the capability of the system in vibrating a moving magnet fixed onto a silicone phantom at the target frequency with a torsional efficiency always above 0.82, thus extending our previous studies that included static magnets only (Figure 4).^[17,18] Moreover, the video analysis showed that the vibrations at 40 μNm led to magnet displacements up to $\approx 150\ \mu\text{m}$, which already demonstrated to be sufficient to elicit muscle sensory neural responses in an animal model.^[18] These displacements are also comparable with those employed in some noninvasive studies to elicit kinesthetic illusions in targeted sensory reinnervated amputees.^[13,14]

Static tests with one magnet (Test B1) demonstrated a parabolic trend of the median tracking errors ΔE_p and ΔE_o w.r.t. the distance from the sensor boards (Figure 5). The inverse proportionality of the tracking error with the magnet-sensors distance, for low distances, is likely explained by the sensor input saturation and hysteresis effects caused by the high strength of the actuation MFs. Instead, for large distances, the tracking error increased with the distance probably due to the cubic decrease ($1/r^3$) of signal-to-noise ratio of the magnet MF. The error introduced for short distances could be mitigated by sensors with a larger full-scale output. Instead, for large magnet-sensors distances, better signal-to-ratios could be achieved using stronger magnets (higher magnetization or larger volume). Notably, the magnet-sensors distance that yielded the lowest tracking error in Test B1 ($\approx 14\text{--}15\ \text{mm}$) was chosen to further explore the tracking accuracy and precision in the other tests with multiple magnets (B2 and B3).

Altogether, the outcomes of tests B1, B2, and B3 indicate that vibrating the magnets introduces MF disturbances, proportional to the torque amplitude, which are overall limited and still allow for tracking with millimeter accuracy (Figure 5–7). Notably, the pose errors found account only for the deviations introduced by the actuation coils and should be combined with those intrinsic of the reverse optimization algorithm in absence of MF disturbances, which are however an order of magnitude smaller (submillimeter errors). Taken together, the compound error (intrinsic plus actuation) suggest that we can track magnet displacements due to muscle contractions (e.g., around 8 mm if magnets are placed in the muscle belly of sufficiently long residual muscle) with enough fidelity.^[51] These tests also highlighted that there was minimal difference in the accuracy of the tracking algorithm during static (Tests B1, B2) and dynamic tests (Test B3). This finding was possibly related to the slowly moving and gradual motion imposed to the magnets ($1.5\ \text{cm s}^{-1}$). Indeed, previous studies^[34,45] had already characterized the effect of magnets speed in tracking accuracy, precision, and computation time, demonstrating no difference at slow magnets

speed. Although, those studies were conducted in absence of the coil disturbing MFs, we speculate that such a behavior could be representative also in this scenario, including a monotonically increasing error once a certain speed threshold is crossed. Future work could address more thoroughly the impact of magnets speed on the system capability of tracking pose and updating the vibration in the model-based controller, focusing on the speed range of muscle contraction ($2\text{--}50\ \text{cm s}^{-1}$).^[46]

The adopted silicone phantom used in this study exhibited mechanical features comparable to those of the muscular tissue^[48] and was already assessed in our previous study.^[18] Based on our experience with animal tests, gained in vibrating magnets implanted in rodents' paws,^[18] we found this methodology appropriate to test the system functionality and we do not expect significant performance deterioration in a real anatomical configuration in terms of tracking accuracy, precision, and frequency selectivity.

Although the conducted tests demonstrated the system compliance to most of the requirements for a HMI (power consumption, frequency selectivity, and tracking accuracy), the present prototype cannot be embedded in a prosthetic socket for its size and weight. Yet, the actual footprint of the prototype does not prevent its use for bench tests to validate scientific hypotheses on proprioception in humans. Clinical trials will contribute to identify the optimal parameter set (duration, amplitude, and frequency) to elicit movement illusions through our system.

Another limitation of the proposed system is its incompatibility with other medical devices in its proximity (such as pacemakers, cochlear implants), whose functionality maybe be altered by the MF radiated emissions. Further efforts are needed to ensure the electromagnetic compatibility of this device by reducing the unintentional emissions generated by the current drivers and the coils. In contrast, this limitation does not prevent its preliminary use in a clinical trial by appropriately defining the inclusion criteria.

In conclusion, this study provides empirical evidence for the viability of effectively tracking and vibrating multiple remote magnets. These outcomes represent an essential step forward towards the deployment of a novel scientific instrument capable to deliver feedback in persons with implanted magnets in their muscles. In the future, the effectiveness of this device in delivering proprioceptive sensations in amputees will be addressed in clinical trials, whose outcomes may ultimately improve our understanding of the kinesthetic sense. Furthermore, the development of this device holds potential relevance for other scientific domains requiring the simultaneous tracking and manipulation of multiple magnetic targets.

Supporting Information

Supporting Information is available from the Wiley Online Library or from the author.

Acknowledgements

F.M. and E.L.F. contributed equally to this work. The idea of the myokinetic interface was funded by Scuola Superiore Sant'Anna and the European Research Council under the MYKI Project in 2015 (ERC-2015-StG, grant no. 679820).

Conflict of Interest

The authors declare no conflict of interest.

Data Availability Statement

The data that support the findings of this study are available from the corresponding author upon reasonable request.

Keywords

amputation, human machine interface, kinesthesia, magnetic actuation, magnetic tracking, myokinetic stimulation interface, proprioception

Received: November 10, 2023

Revised: January 22, 2024

Published online: March 8, 2024

-
- [1] V. Mendez, F. Iberite, S. Shokur, S. Micera, *Annu. Rev. Control. Robot. Auton. Syst.* **2021**, 4, 595.
- [2] E. Losanno, M. Mender, C. Chestek, S. Shokur, S. Micera, *Nat. Rev. Bioeng.* **2023**, 1, 390.
- [3] M. Gherardini, F. Masiero, V. Ianniciello, C. Cipriani, *Curr. Opin. Biomed. Eng.* **2023**, 27, 100460.
- [4] N. Parajuli, N. Sreenivasan, P. Bifulco, M. Cesarelli, S. Savino, V. Niola, D. Esposito, T. J. Hamilton, G. R. Naik, U. Gunawardana, G. D. Gargiulo, *Sensors* **2019**, 19, 4596.
- [5] J. W. Sensinger, S. Dosen, *Front. Neurosci.* **2020**, 14, 345.
- [6] F. Clemente, M. D'Alonzo, M. Controzzi, B. B. Edin, C. Cipriani, *IEEE Trans. Neural Syst. Rehabil. Eng.* **2015**, 24, 1314.
- [7] G. Gu, N. Zhang, H. Xu, S. Lin, Y. Yu, G. Chai, L. Ge, H. Yang, Q. Shao, X. Sheng, X. Zhu, X. Zhao, *Nat. Biomed. Eng.* **2021**, 7, 589.
- [8] D. W. Tan, M. A. Schiefer, M. W. Keith, J. R. Anderson, J. Tyler, D. J. Tyler, *Sci. Transl. Med.* **2014**, 6, 257ra138.
- [9] S. Raspopovic, M. Capogrosso, F. M. Petrini, M. Bonizzato, J. Rigosa, G. Di Pino, J. Carpaneto, M. Controzzi, T. Boretius, E. Fernandez, G. Granata, C. M. Oddo, L. Citi, A. L. Ciancio, C. Cipriani, M. C. Carrozza, W. Jensen, E. Guglielmelli, T. Stieglitz, P. M. Rossini, S. Micera, *Sci. Transl. Med.* **2014**, 6, 222ra19.
- [10] J. A. George, D. T. Kluger, T. S. Davis, S. M. Wendelken, E. V. Okorokova, Q. He, C. C. Duncan, D. T. Hutchinson, Z. C. Thumser, D. T. Beckler, P. D. Marasco, S. J. Bensmaia, G. A. Clark, *Sci. Robot.* **2019**, 4, aax2352.
- [11] E. Mastinu, L. F. Engels, F. Clemente, M. Dione, P. Sassu, O. Aszmann, R. Brånemark, B. Håkansson, M. Controzzi, J. Wessberg, C. Cipriani, M. Ortiz-Catalan, *Sci. Rep.* **2020**, 10, 11793.
- [12] G. M. Goodwin, D. I. McCloskey, P. B. C. Matthews, *Science* **1972**, 175, 1382.
- [13] P. D. Marasco, J. S. Hebert, J. W. Sensinger, C. E. Shell, J. S. Schofield, Z. C. Thumser, R. Nataraj, D. T. Beckler, M. R. Dawson, D. H. Blustein, S. Gill, B. D. Mensh, R. Granja-Vazquez, M. D. Newcomb, J. P. Carey, B. M. Orzell, *Sci. Transl. Med.* **2018**, 10, eaa06990.
- [14] P. D. Marasco, J. S. Hebert, J. W. Sensinger, D. T. Beckler, Z. C. Thumser, A. W. Shehata, H. E. Williams, K. R. Wilson, *Sci. Robot.* **2021**, 6, abf3368.
- [15] S. Tarantino, F. Clemente, D. Barone, M. Controzzi, C. Cipriani, *Sci. Rep.* **2017**, 7, 17149.
- [16] S. Milici, M. Gherardini, F. Clemente, F. Masiero, P. Sassu, C. Cipriani, *IEEE Trans. Neural Syst. Rehabil. Eng.* **2020**, 28, 2451.
- [17] J. Montero, F. Clemente, C. Cipriani, *Sci. Rep.* **2021**, 11, 15456.
- [18] J. Montero, Z. C. Thumser, F. Masiero, D. T. Beckler, F. Clemente, P. D. Marasco, C. Cipriani, *J. Neural Eng.* **2022**, 19, 26048.
- [19] J. J. Abbott, E. Diller, A. J. Petruska, *Annu. Rev. Control. Robot. Auton. Syst.* **2020**, 3, 57.
- [20] Z. Yang, L. Zhang, *Adv. Intell. Syst.* **2020**, 2, 2000082.
- [21] M. P. Kummer, J. J. Abbott, B. E. Kratochvil, R. Borer, A. Sengul, B. J. Nelson, *IEEE Trans. Robot.* **2010**, 26, 1006.
- [22] F. Ongaro, S. Pane, S. Scheggi, S. Misra, *IEEE Trans. Robot.* **2018**, 35, 174.
- [23] F. N. Piñan Basualdo, S. Misra, *Adv. Intell. Syst.* **2023**, 2300365.
- [24] J. Sikorski, A. Denasi, G. Bucchi, S. Scheggi, S. Misra, *IEEE/ASME Trans. Mechatron.* **2019**, 24, 505.
- [25] S. Pane, V. Iacovacci, E. Sinibaldi, A. Menciassi, *Appl. Phys. Lett.* **2021**, 118, 14102.
- [26] Q. Wang, K. F. Chan, K. Schweizer, X. Du, D. Jin, S. C. H. Yu, B. J. Nelson, L. Zhang, *Sci. Adv.* **2021**, 7, abe5914.
- [27] A. Azizi, C. C. Tremblay, K. Gagné, S. Martel, *Sci. Robot.* **2019**, 4, aax7342.
- [28] Y. Kim, E. Genevriere, P. Harker, J. Choe, M. Balicki, R. W. Regenhardt, J. E. Vranic, A. A. Dmytriw, A. B. Patel, X. Zhao, *Sci. Robot.* **2022**, 7, abg9907.
- [29] J. Rahmer, C. Stehning, B. Gleich, *Sci. Robot.* **2017**, 2, aal2845.
- [30] M. E. Tiryaki, M. Sitti, *Adv. Intell. Syst.* **2022**, 4, 2100178.
- [31] M. E. Tiryaki, Y. G. Elmacioglu, M. Sitti, *Sci. Adv.* **2023**, 9, adg6438.
- [32] S. Tarantino, F. Clemente, A. De Simone, C. Cipriani, *IEEE Trans. Biomed. Eng.* **2019**, 67, 1282.
- [33] M. A. Khan, J. Sun, B. Li, A. Przybysz, J. Kosel, *Eng. Res. Express* **2021**, 3, 22005.
- [34] F. Masiero, E. Sinibaldi, F. Clemente, C. Cipriani, *IEEE Sens. J.* **2021**, 21, 22603.
- [35] M. Gherardini, A. Mannini, C. Cipriani, *Comput. Methods Programs Biomed.* **2021**, 211, 106407.
- [36] S. L. Charreyron, Q. Boehler, B. Kim, C. Weibel, C. Chautems, B. J. Nelson, *IEEE Trans. Robot.* **2021**, 37, 1009.
- [37] K. M. Popek, T. Hermans, J. J. Abbott, in *IEEE Int. Conf. on Robotics and Automation (ICRA)*, Singapore, May **2017**, pp. 1154–1160.
- [38] A. Z. Taddese, P. R. Slawinski, M. Pirota, E. De Momi, K. L. Obstein, P. Valdastri, *Int. J. Rob. Res.* **2018**, 37, 890.
- [39] J. W. Martin, B. Scaglioni, J. C. Norton, V. Subramanian, A. Arezzo, K. L. Obstein, P. Valdastri, *Nat. Mach. Intell.* **2020**, 2, 595.
- [40] D. Son, X. Dong, M. Sitti, *IEEE Trans. Robot.* **2018**, 35, 343.
- [41] D. Son, H. Gilbert, M. Sitti, *Soft Robot.* **2020**, 7, 10.
- [42] I. S. M. Khalil, A. Adel, D. Mahdy, M. M. Micheal, M. Mansour, N. Hamdi, S. Misra, *APL Bioeng.* **2019**, 3, 26104.
- [43] Y. Xu, K. Li, Z. Zhao, M. Q.-H. Meng, *IEEE Trans. Autom. Sci. Eng.* **2020**, 18, 1640.
- [44] M. Zhang, L. Yang, C. Zhang, Z. Yang, L. Zhang, *IEEE Trans. Instrum. Meas.* **2023**, 72, 1.
- [45] V. Ianniciello, M. Gherardini, C. Cipriani, *IEEE Trans. Biomed. Eng.* **2023**, 71, 1068.
- [46] C. Häger-Ross, M. H. Schieber, *J. Neurosci.* **2000**, 20, 8542.
- [47] F. Devernay, *C/C++ Minpack* **2007**, <https://devernay.github.io/cminpack/>.
- [48] J. L. Sparks, N. A. Vavalle, K. E. Kasting, B. Long, M. L. Tanaka, P. A. Sanger, K. Schnell, T. A. Conner-Kerr, *Adv. Skin Wound Care* **2015**, 28, 59.
- [49] P. E. Dupont, B. J. Nelson, M. Goldfarb, B. Hannaford, A. Menciassi, M. K. O'Malley, N. Simaan, P. Valdastri, G.-Z. Yang, *Sci. Robot.* **2021**, 6, abi8017.
- [50] B. Gleich, I. Schmale, T. Nielsen, J. Rahmer, *Science* **2023**, 380, 966.
- [51] F. Paggetti, M. Gherardini, A. Lucantonio, C. Cipriani, *IEEE Trans. Biomed. Eng.* **2023**, 70, 2972.